

A global comparison of V_p , V_s , and V_p/V_s structures of the mantle lithosphere beneath major cratons

Ehsan BARZGAR^{1*}, Fenglin NIU^{1,2} & Shunping PEI³

¹ State Key Laboratory of Petroleum Resources and Prospecting, Unconventional Petroleum Research Institute, China University of Petroleum, Beijing 102249, China;

² Department of Earth, Environmental and Planetary Sciences, Rice University, Houston 77005, Texas, USA;

³ State Key Laboratory of Tibetan Plateau Earth System and Resources Environment, Institute of Tibetan Plateau Research, Chinese Academy of Sciences, Beijing 100101, China

Received June 12, 2022; revised September 13, 2022; accepted October 26, 2022; published online January 13, 2023

Abstract Cratons formed due to the specific melting regime of the primitive mantle with elevated mantle temperature during Archean. However, each craton has undergone a distinct evolution history, and some have lost their stability. To investigate to what degree cratons in comparison with one another have been modified from their analogous initial form, we employed Sn-Pn differential (PSn) traveltimes to derive V_p/V_s ratio, which is thought to be related to Mg# of the uppermantle. We assessed Pn, Sn, and PSn data using three datasets based on epicentral distance: (1) 2°–12°, (2) 2°–7°, and (3) 7°–12°. The results suggest that most cratons show comparable seismic properties with high velocities and low V_p/V_s ratio, implying a highly depleted uppermost mantle that resembles the original residue from the partial melt extraction of the primitive mantle during the Archean. Conversely, the Eastern North China Craton (ENCC) displays the lowest P- and S-wave velocities, and noticeable high V_p/V_s ratios in all datasets, implying a systematic difference with other cratons. This observation suggests a scenario of total removal of the depleted Archean mantle lithosphere beneath the ENCC. In contrast, the Ordos Block located at the western part of the North China Craton (WNCC) shows velocities and V_p/V_s ratio comparable with those of the typical cratons, suggesting that it has still maintained its Archean mantle lithosphere. The Wyoming Craton has a high V_p/V_s ratio similar to that of the ENCC and a high P-wave velocity comparable to that of the typical cratons. These features suggest that the Archean mantle lithosphere has been significantly modified rather than totally removed and replaced by a younger fertile mantle. The Indian Craton presents a low V_p/V_s ratio and comparatively high velocities at shallow parts of the mantle lithosphere but a high V_p/V_s ratio at deeper parts similar to that of the ENCC, suggesting a partial modification of the Indian Craton at deeper parts.

Keywords Craton, Craton modification, Mantle lithosphere, North China Craton, Wyoming Craton, Indian Craton, V_p/V_s ratio, Seismic velocity

Citation: Barzgar E, Niu F, Pei S. 2023. A global comparison of V_p , V_s , and V_p/V_s structures of the mantle lithosphere beneath major cratons. Science China Earth Sciences, 66, <https://doi.org/10.1007/s11430-022-1023-x>

1. Introduction

Cratons recall stability. However, there are cratons such as the Eastern North China Craton (ENCC) and the Wyoming Craton that contradict this general thought, manifested by

thin lithosphere, extensive magmatism, and ductile deformation (Zhu et al., 2012; Niu et al., 2015; Wu et al., 2019; Pearson et al., 2021). Cratons possess giant mineral deposits such as gold and diamond (Zhu et al., 2017; Pearson et al., 2021), and thus understanding their structure, formation, and evolution is worthwhile. In addition, they are crucial to decipher Earth's early history as it is believed that cratons were

* Corresponding author (email: ehsan.barzgar@gmail.com)

resulted during the Archean when the mantle temperature was elevated (Carlson et al., 2005; Shulgin and Artemieva, 2019). This specific condition was accompanied by a distinctive high-degree melt extraction regime forming a unique residue with a strong, viscous, and depleted nature (Carlson et al., 2005; Shulgin and Artemieva, 2019). Then, this unique residue was drifted and assembled several times during its billion-year life span, and each part has undergone and is marked by an exclusive history. Thus, a comparison of the current characteristics of the cratons can tell us the long varying story of each craton as well as how much each craton has been modified since the Archean.

To compare the properties of cratons and contrast potential modifications, various methods have been employed, and each has certain limitations. Mantle xenolith studies provide valuable information about the nature of cratons, but one should take precautions when interpreting them: First, they are limited in temporal and spatial coverage, particularly at the shallow parts of the mantle lithosphere. Second, cratonic blocks have not been studied equally, and some of them, such as the Yilgarn Craton and the Ordos Block of the NCC, lack xenolith records. Third, a recent study (Artemieva et al., 2019) suggests that they might not be representative of the cratons, as they were modified by large-scale magmatism prior to or during the eruption. Global and regional seismic studies are other tools for inferring the differences among cratons. However, distinguishing thermal, compositional, fluid and melt presence, and other effects on seismic velocity is challenging and controversial (Artemieva, 2009). Furthermore, the non-uniqueness of the tomography results as well as the parameterization and the regularization employed in tomography methods somewhat complicate a fair comparison of cratons. Therefore, establishing a consistent approach among cratons can better unravel the differences among them.

Due to their depleted nature as well as cold temperature, cratons possess higher velocities and lower V_p/V_s ratio compared with younger neighboring terrains (James et al., 2004; Niu et al., 2004). Meanwhile, destructive processes such as metasomatism can modify the original unique characteristics of the mantle lithosphere, which once were responsible for the long-term stability of the cratons. These modifications reduce the Mg# ($100 \times \text{Mg}/(\text{Mg}+\text{Fe})$) as well as modify the modal composition by increasing pyroxene-rich contents and lowering olivine content, which generally results in lower velocities and higher V_p/V_s ratio (Lee, 2003; Carlson et al., 2005; Artemieva, 2009; Shulgin and Artemieva, 2019). Thus, velocity and in particular V_p/V_s ratio, which is more sensitive to Mg# than to temperature (Lee, 2003), can be used to constrain the degree of modification among various cratons. Here we employ Pn and Sn waves that propagate through the uppermost mantle to investigate average velocity structure and V_p/V_s ratio beneath 11 major

cratons around the world to examine the potential modification of each craton.

Logically, the uppermost mantle lithosphere should be less modified than its base because it is farther from destructive processes such as asthenospheric and mantle plume activities, ascending slab fluids, and basal drag stresses. Indeed, several studies confirmed that lithospheric modification and consequent thinning are somewhat pervasive at the base of the cratons, albeit with various scales (Wu et al., 2014; Hu et al., 2018; Celli et al., 2020). However, seismic observations appear to be less obvious and also not always align with xenolith data (Bruneton et al., 2004; Lebedev et al., 2009; Pedersen et al., 2009; Eeken et al., 2018). To better constrain depth variations of velocity structure, we divided Pn and Sn data into two distance ranges: $2^\circ\text{--}7^\circ$ and $7^\circ\text{--}12^\circ$, which travel in different depths of the mantle lithosphere.

Seismic studies generally suggest a thick lithosphere with a comparatively homogenous high velocity down to depths of ~ 200 km for cratons of the world (Shapiro and Ritzwoller, 2002; Pearson et al., 2021). NCC, however, is an exception with an extremely heterogeneous nature in both vertical and horizontal directions throughout its entire lithosphere from the crust to the lithosphere-asthenosphere boundary (LAB) (Chen et al., 2008, 2009; Zheng et al., 2012; Jiang et al., 2013; Xu et al., 2018; Lü, 2019; Lü et al., 2020). The Moho and LAB depths vary sharply in the range of $\sim 27\text{--}45$ and $\sim 70\text{--}200$ km, respectively (Chen et al., 2008, 2009; Zhu et al., 2012). Generally, the seismic structures throughout the entire lithosphere are more homogenous in the Ordos Block of the Western North China Craton (WNCC) compared with the ENCC (Zhu et al., 2012), although recent seismic studies suggest ongoing modification of the Ordos Block at its peripheries (Yu and Chen, 2016; Lü et al., 2020). Some seismic studies (e.g., Lei et al., 2020) suggest small-scale delamination at shallow depths of ~ 100 km, implying a continuing destruction process of the NCC since the Late Mesozoic. Larger-scale delaminated objects have also been detected at greater depths down to the base of the mantle transition zone within the NCC, suggesting possible large-scale removal of the Archean lithosphere in the past (Lei, 2012; Zuo et al., 2020). Moreover, several studies show mantle upwelling in various parts of the NCC, particularly within the Trans-North China Orogen (TNCO) and the ENCC, which some were suggested to be originated from deeper parts of the upper mantle (Zhao et al., 2009; Lei, 2012; Zhao et al., 2012).

The main focus of this research is to compare the modification degree of cratons, particularly the so-called “modified cratons” such as the ENCC, Wyoming, and Indian Craton, which is a controversial topic, as their modification degree is up to debate. For example, despite numerous studies for unraveling the degree of modification beneath the ENCC, whether or not the whole ancient lithospheric keel

has been removed beneath the ENCC remains obscure. The comparison of the Paleozoic kimberlites and the Cenozoic basalts indicates that the ENCC lost around 100 km of its root (Zhu et al., 2012; Niu et al., 2015; Wu et al., 2019; Xu et al., 2019). It also shows that the nature of the mantle lithosphere beneath the ENCC changed from depleted ($Mg\# > 92$) to fertile ($Mg\# \sim 89-90$) (Zheng et al., 2007). These features suggest the removal and replacement of the mantle lithosphere occurred between these two periods, although the scale of this removal is up to debate. The Wyoming Craton is another example of the modified cratons with controversies on its modification degree. For example, a xenoliths study (Carlson et al., 2004) inferred a younger layer underlying an Archean one based on a few samples at the edges of the craton. However, recent seismic studies (e.g., Humphreys et al., 2015; Golos et al., 2020) show somewhat high-velocity anomalies down to at least depths of ~ 200 km, implying the presence of the Archean mantle lithosphere beneath it. Another example of modified cratons is the Indian Craton. A recent xenoliths study (Dessai et al., 2021) suggests that the western parts of the Indian Craton lost parts of its lithospheric root. Furthermore, some seismic studies suggest a somewhat thin lithosphere for parts of the Indian Craton (e.g., Maurya et al., 2016). In contrast to the modified cratons, typical cratons such as the Superior Craton are generally thought to be intact unmodified cratons manifested by their thick lithosphere, low seismicity, and low deformation. However, some studies suggest that they were modified at some parts, particularly at their margins (Wang et al., 2016). For example, xenoliths analysis suggests that parts of the Superior Craton had been modified during the Midcontinent Rifting (Smit et al., 2014). Here we try to resolve the modification degree for both so-called “modified cratons” and “typical cratons” through a consistent comparison between them.

2. Data

We collected Pn and Sn data that sample the NCC, Superior, Wyoming, Yilgarn, Kalahari, East European, Siberian, Indian, and Tanzania Cratons (Figure 1). The cratonic blocks here mainly include Archean crustal parts, except for the East European Craton, which also includes major Paleoproterozoic crustal parts. Sufficient ray coverage was the main priority for selecting these cratons. For example, we skipped Slave, Congo, South American, and West African Cratons due to insufficient ray coverage. More importantly, we discarded off-cratonic areas in the ray selection process for each craton to ensure that the majority of the rays were passing within the uppermost mantle of the on-cratonic area. In addition, for a consistent analysis, we employed the same cratonic area for each craton for different phases and data

subsets. To maintain a comprehensive analysis, we chose both typical and modified cratons. The three parts of the NCC are the ENCC, the TNCO, and the WNCC. The Indian Craton comprises the Dharwar, Bastar, and Singhbhum Cratons, as well as the Deccan Traps. The Siberian Craton here only includes the Aldan Shield. The East European Craton includes the Archean Kola and Karelia Cratons, as well as the Paleoproterozoic Baltic Shield and the East European Platform (Artemieva et al., 2006). The Kalahari Craton consists of the Kaapvaal and Zimbabwe Cratons with the Bushfield between them.

For the NCC, we extracted Pn and Sn traveltimes data in the distance range of $2^\circ-12^\circ$ from the Annual Bulletin of Chinese Earthquakes (ABCE) between 1985 and 2019. For the other cratons, we extracted data from ISC-Reviewed and ISC-EHB Bulletins between 1964 and 2018, as well as from the ISC Bulletin between 2018 and 2020. We removed all earthquakes with hypocenters located beneath the Moho given by the CRUST 1.0 model (Laske et al., 2013). We also discarded duplicated data when we combined different catalog data. The total numbers of Pn and Sn traveltimes data are 178,585 and 67,359, among which 53,774 event-station pairs have both Pn and Sn picks, allowing to obtain Sn-Pn differential traveltimes that are insensitive to origin time errors. Here we assume that Pn and Sn of an event-station pair share the same raypath and define a pseudowave, referred to as PSn, that travels along the same raypath with a traveltimes equivalent to the Sn-Pn differential time. Figure S1 in the Supplementary materials (<https://link.springer.com>) shows the PSn ray coverage and count in a $0.5^\circ \times 0.5^\circ$ bin across the 11 cratonic blocks. It should be noted that the Pn and Sn ray coverages are denser than those of the PSn. More details on the raypath counts at each craton are listed in Table 1. Note that we conducted three separate regressions for the three datasets, which resulted in a slightly different number of outliers based on a fixed threshold.

3. Method

A Pn (or Sn) raypath consists of three segments: crustal segment from the source to the mantle, the subhorizontal segment through the mantle, and the crustal segment from mantle to the receiver (e.g., Hearn et al., 1991). The Pn (or Sn) traveltimes thus can be written as:

$$t = a + b + D\bar{S}, \quad (1)$$

where a and b are referred to as the event and station static delays, respectively. D is the epicentral distance and \bar{S} is the slowness averaged along the mantle ray segment. For each cratonic block, if we assume velocity structure within the uppermost mantle is relatively even laterally, then eq. (1) shows that Pn (or Sn) traveltimes is a linear function of epi-

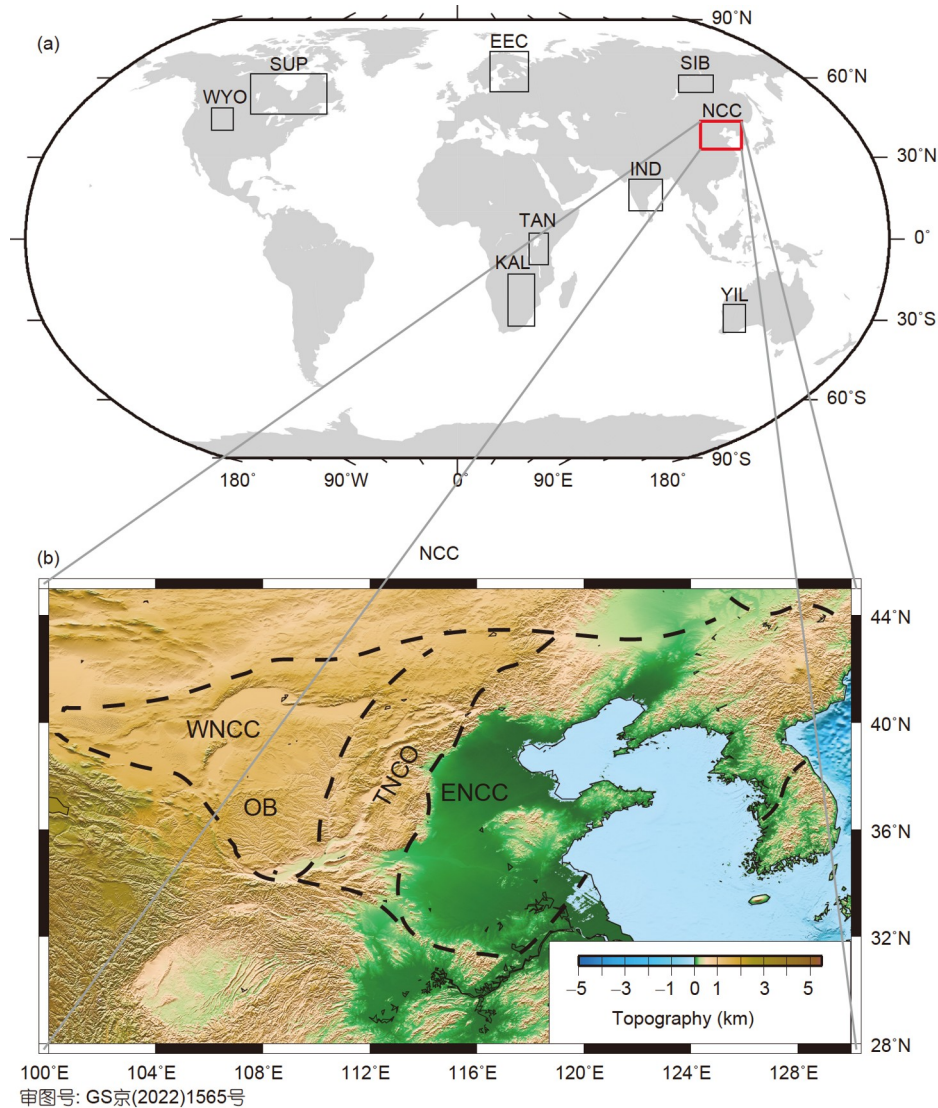


Figure 1 Map showing the approximate locations of the selected cratons, as well as a topographic map of the North China Craton (NCC). (a) Approximate locations of the cratons. The abbreviations in the map stand as follows: SIB, Aldan Shield of the Siberian Craton; IND, Indian Craton; YIL, Yilgarn Craton; TAN, Tanzania Craton; KAL, Kalahari Craton; EEC, East European Craton; SUP, Superior Craton; WYO, Wyoming Craton. (b) Topographic map of the NCC with its subdivisions. ENCC, TNCO, WNCC, and OB denote Eastern NCC, Trans North China Orogen, Western part of the NCC, and Ordos Block, respectively. Dashed lines mark the outlines of the NCC and its subdivisions.

Table 1 The number of Pn, Sn, and pseudowave (PSn) rays in full-, short-, and long-distance datasets

Cratons	PSn			Pn			Sn		
	Full	Short	Long	Full	Short	Long	Full	Short	Long
SIB	1910	1887	–	4510	4369	–	2653	2611	–
ENCC	2500	2441	74	14973	14624	264	3028	2956	67
TNCO	540	538	–	3022	2967	–	715	710	–
WNCC	814	811	–	2432	2429	–	926	922	–
IND	823	576	247	1202	847	355	1087	755	336
YIL	1663	1571	–	2631	2516	–	1992	1881	–
TAN	559	391	–	965	699	–	692	493	–
KAL	5779	5138	639	6954	6251	701	6368	5733	652
EEC	32676	27150	5349	64054	51952	10266	42092	35806	5877
SUP	4402	3497	904	7620	6302	1327	5225	4120	1114
WYO	2108	2105	–	70222	70137	–	2581	2574	–

central distance with a slope equal to the average slowness, i.e., the inverse of the apparent velocity. A linear regression thus can be used to determine the average slowness of the uppermost mantle. The linear regression, however, can be affected by the two static terms, as the event static term varies from earthquakes to earthquakes due to different focal depths while the station term changes with station elevation. Therefore, it is necessary to make corrections on event depth and receiver elevation. For source-station pair, we made a source and station traveltimes correction by projecting the hypocenter and station to the surface at sea level. The source and station static corrections are:

$$\begin{cases} a_c = z \cdot \sqrt{\frac{1}{v_c^2} - \frac{1}{v_m^2}}, \\ b_c = -h \cdot \sqrt{\frac{1}{v_{uc}^2} - \frac{1}{v_m^2}}, \end{cases} \quad (2)$$

where z and h are focal depth and station elevation in kilometers. v_c , v_{uc} , and v_m are the average crustal, upper crust, and uppermost mantle velocities, respectively. We assumed $v_c = 6.4 \text{ km s}^{-1}$, $v_{uc} = 5.5 \text{ km s}^{-1}$, and $v_m = 8.1 \text{ km s}^{-1}$ for P wave and $v_c = 3.7 \text{ km s}^{-1}$, $v_{uc} = 3.1 \text{ km s}^{-1}$, and $v_m = 4.6 \text{ km s}^{-1}$ for S wave. The corrected times were updated several times by replacing the v_m with the inverse slope of the regression process. Let T to be corrected traveltimes, i.e., $T = t + a_c + b_c$, then we can write eq. (1) into:

$$T = D\bar{S} + c, \quad (3)$$

Here, c is the sum of the static delays and corrected times. i.e., $c = a + b + a_c + b_c$.

Once the source and station statics are corrected, we employed standard linear regression to estimate the average slowness and the associated standard deviation (e.g., [Montgomery and Runger, 2011](#)):

$$\begin{cases} \bar{S} = \sum_{i=1}^n (D_i - \bar{D})(T_i - \bar{T}) / \sum_{i=1}^n (D_i - \bar{D})^2, \\ \text{Var}(\bar{S}) = \frac{1}{n-1} \sum_{i=1}^n [T_i - (\bar{S}D_i + \hat{c})]^2 / \sum_{i=1}^n (D_i - \bar{D})^2, \end{cases} \quad (4)$$

where \bar{S} and \hat{c} are the linear least-square fits of the slowness and crustal traveltimes. \bar{D} and \bar{T} are averaged epicentral distance and corrected traveltimes, respectively. The average Pn velocity (\bar{V}_{Pn}) and Sn (\bar{V}_{Sn}) are then estimated from their corresponding linear least-square fits of the slowness (\bar{S}_P, \bar{S}_S): $\bar{V}_{Pn} = 1 / \bar{S}_P$ and $\bar{V}_{Sn} = 1 / \bar{S}_S$. For the PSn traveltimes data (i.e., Sn-Pn differential traveltimes), we also employed its linear least-square fitted apparent slowness to compute an apparent PSn velocity, $\bar{V}_{PSn} = 1 / \bar{S}_{PS}$, which can be used to compute V_p/V_s ratio:

$$V_p/V_s = 1 + \bar{V}_{Pn} \cdot \bar{S}_{PS}. \quad (5)$$

During the regression, we discarded outliers with a tra-

veltime residual greater than 12 s for PSn, 10 s for Sn, and 7 s for Pn. In determining these threshold values, our primary objective was to increase high-quality rays without allowing outliers to deviate the results. Thus, we tested several thresholds and chose the above values that satisfy the mentioned criteria among cratons.

Considering Earth's sphericity and the fact that longer Pn/Sn rays dive into the deeper parts of the mantle lithosphere, the average apparent velocity depends slightly on the epicentral distance ([Hearn et al., 2019](#)). Therefore, we further divided the full-distance range (2° – 12°) into short-distance (2° – 7°) and long-distance (7° – 12°) ranges. If sufficient traveltimes data are available in each distance range, we further applied the linear regression analysis to the sub dataset. The depth estimation of the mentioned datasets might slightly vary among cratons as well as within a craton itself. We followed [Hearn et al. \(2019\)](#) and estimated the depth sensitivity of each dataset. Assuming an average cratonic model (further details are provided in the Supplementary materials), we approximated an average sampling depth of 56, 44, and 62 km for Pn phase using the full-, short-, and long-distance datasets. Similarly, the corresponding average depths for the Sn phase are 70, 48, and 78 km.

4. Results

The regression results of PSn traveltimes from the 11 cratonic blocks are shown in [Figure 2](#), with the left, middle and right columns showing the traveltimes fitting, traveltimes residual, and histograms of traveltimes residuals. Similar plots for the Pn and Sn data are shown in [Figures S2 and S3](#), respectively. [Table 2](#) listed the estimated apparent velocity of the Pn, Sn, and pseudo PSn waves of the 11 cratons derived from the full-, short- and long-distance traveltimes datasets. [Figure 3](#) displays the V_p/V_s ratio, V_{Pn} , V_{Sn} , and V_{PSn} of the cratons using the short- and full-distance datasets. Except for the ENCC, TNCO, Wyoming, and comparatively East European Cratons, other cratons approximately lie within comparable ranges. For example, except for the mentioned outliers, the V_p/V_s ratio of the cratons is ~ 1.72 – 1.75 using the short-distance dataset. In both datasets, the ENCC displays the lowest velocities as well as high V_p/V_s ratios of ~ 1.77 – 1.78 . The TNCO shows values between those of the ENCC and the WNCC. The Wyoming Craton has a high V_p/V_s ratio of ~ 1.78 , comparable with that of the ENCC. In addition, it has a high P-wave velocity of $\sim 8.08 \text{ km s}^{-1}$, close to that of the typical cratons.

[Figure 4](#) shows the V_p/V_s ratio in correlation with the S- and P-wave velocities of the cratons using the full- and the short-distance datasets. As illustrated in [Figure 4a and 4b](#), the ENCC and the Wyoming Craton with high V_p/V_s ratio as well as low S-wave velocity clearly distinguish themselves from

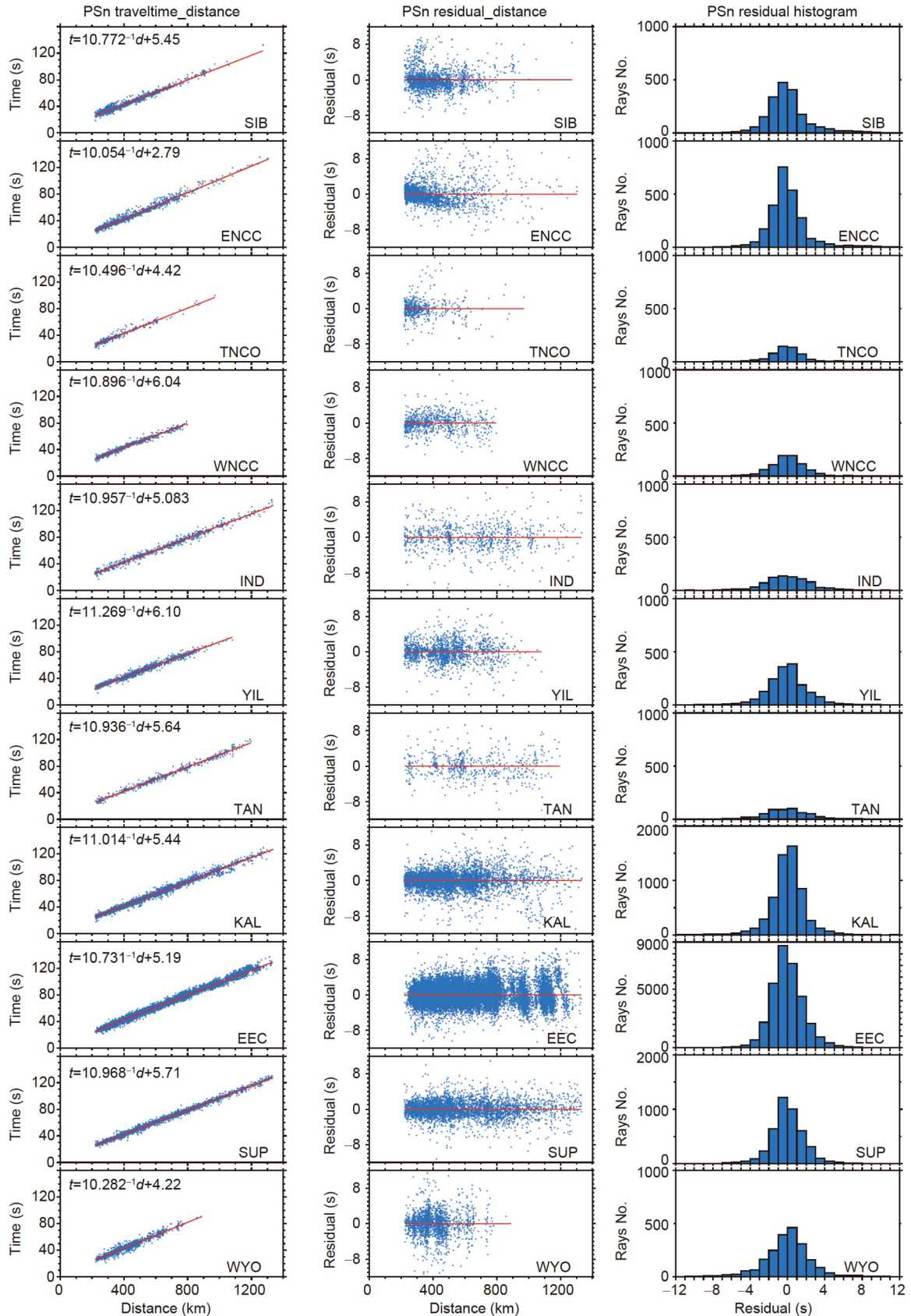


Figure 2 Pseudowave (PSn) traveltime versus distance (left panel), PSn residual versus distance (middle panel), and PSn residual histograms (right panel) of the full-distance datasets. Blue dots in the left and middle panels represent the observed Sn-Pn differential traveltimes after the static corrections. The red lines in the left panel are the linear least-square fits of the PSn traveltime data. The associated cratonic block of each figure is denoted at the corner.

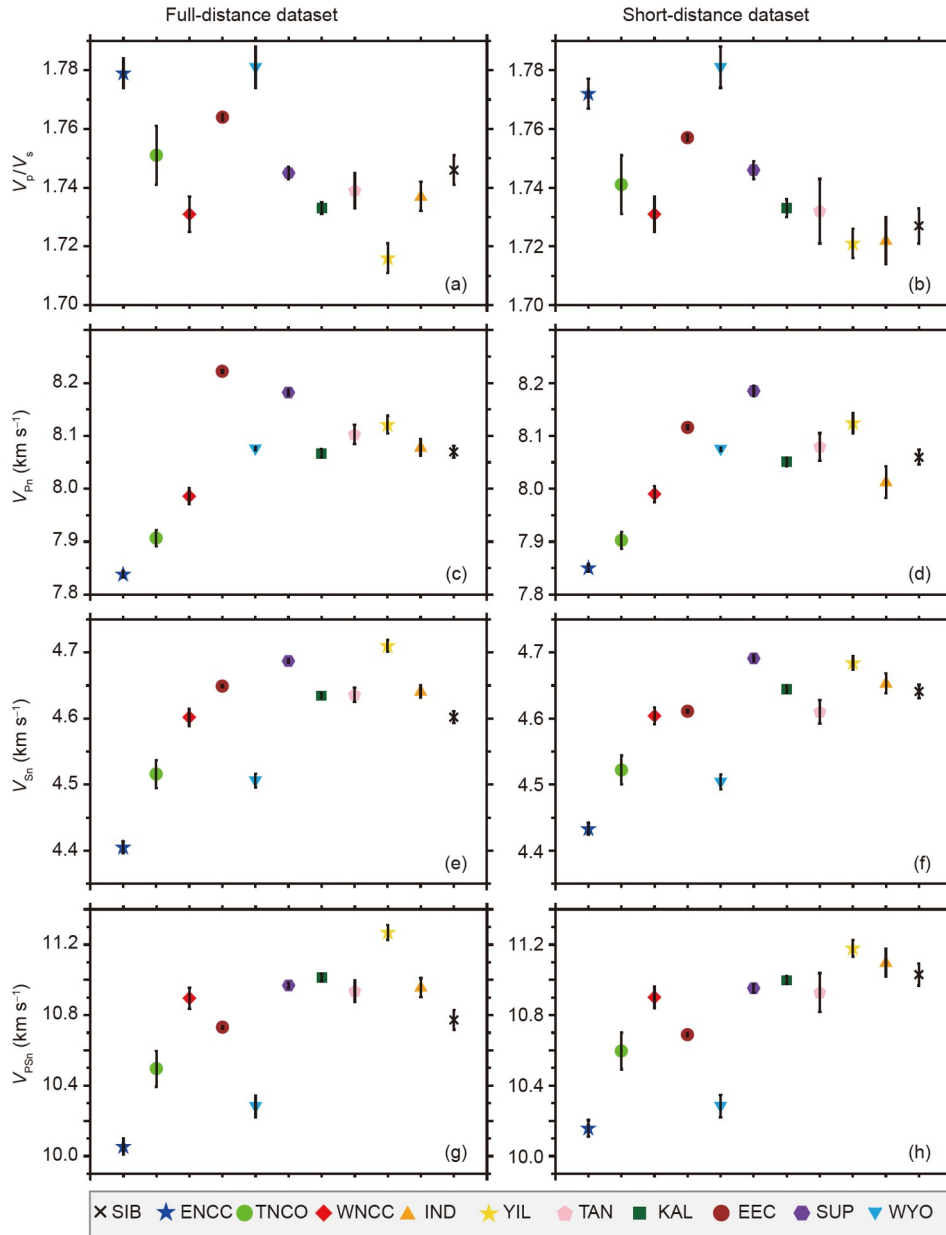


Figure 3 Comparison of the seismic properties (V_p/V_s , V_{Pn} , V_{Sn} , V_{PSn}) of the cratons derived from the full-distance (left panel) and short-distance datasets (right panel). Full-distance and short-distance datasets refer to the traveltimes observed in the distance range of 2° – 12° and 2° – 7° , respectively. Note the contrasting seismic properties of the ENCC in all properties compared with those of the other cratons. The Wyoming Craton shows a noticeably high V_p/V_s ratio ((a) and (b)) and high V_{Pn} ((c) and (d)).

other cratons. On the other hand, typical cratons such as the Yilgarn Craton present high velocities and low V_p/V_s ratio.

Figure 5 displays the seismic properties of the cratons using the short- and long-distance datasets. Using the short-distance dataset, the Indian Craton shows a low V_p/V_s ratio of ~ 1.72 and high velocities, similar to those of the typical cratons, while its V_p/V_s ratio using the long-distance dataset changes significantly to ~ 1.79 , similar to that of the ENCC. The P- and S-wave velocities of the Kalahari and East European Cratons increase from short- to long-distance datasets, whereas the S-wave velocity of the Superior Craton decreases, and its P-wave velocity slightly changes.

<https://engine.scichina.com/doi/10.1007/s11430-022-1023-x>

5. Discussion

5.1 Reliability of the results

We followed several procedures and tests to ensure the validity of our results. As shown in Figures 2, S2, and S3, the traveltime residuals follow the Gaussian distribution, suggesting the traveltime data can be fitted reasonably well by straight lines. As mentioned earlier, to ensure the reliability of the results we tested several residual thresholds for outliers and found that lower thresholds also yielded consistent results. For example, results computed with an outlier threshold of 10 s for PSn, 8 s for Sn, and 5 s for Pn are shown in Table S1 in the

Table 2 The apparent velocity of the Pn, Sn, and pseudowave (PSn) rays in full-, short-, and long-distance datasets

Cratons	V_{PSn} (km s ⁻¹)			V_{Pn} (km s ⁻¹)			V_{Sn} (km s ⁻¹)		
	Full	Short	Long	Full	Short	Long	Full	Short	Long
SIB	10.772±0.055	11.030±0.063	–	8.068±0.011	8.059±0.014	–	4.602±0.009	4.641±0.010	–
ENCC	10.054±0.045	10.157±0.047	9.958±0.288	7.838±0.006	7.850±0.007	7.742±0.054	4.405±0.009	4.433±0.009	4.395±0.063
TNCO	10.496±0.102	10.596±0.104	–	7.907±0.015	7.902±0.016	–	4.516±0.021	4.522±0.022	–
WNCC	10.896±0.060	10.901±0.062	–	7.986±0.015	7.990±0.015	–	4.602±0.013	4.604±0.013	–
IND	10.957±0.053	11.097±0.078	10.489±0.183	8.080±0.016	8.012±0.030	8.184±0.071	4.640±0.009	4.653±0.015	4.593±0.035
YIL	11.269±0.042	11.179±0.047	–	8.121±0.017	8.124±0.019	–	4.710±0.009	4.684±0.010	–
TAN	10.936±0.060	10.927±0.110	–	8.106±0.018	8.079±0.026	–	4.635±0.011	4.611±0.018	–
KAL	11.014±0.021	10.998±0.022	11.374±0.115	8.063±0.008	8.051±0.008	8.285±0.043	4.634±0.004	4.646±0.005	4.690±0.029
EEC	10.731±0.007	10.689±0.009	10.891±0.034	8.222±0.002	8.116±0.003	8.422±0.009	4.649±0.001	4.611±0.002	4.742±0.007
SUP	10.968±0.015	10.952±0.025	10.697±0.057	8.182±0.006	8.185±0.010	8.220±0.027	4.687±0.003	4.691±0.005	4.636±0.013
WYO	10.282±0.062	10.284±0.064	–	8.076±0.003	8.075±0.003	–	4.506±0.010	4.504±0.011	–

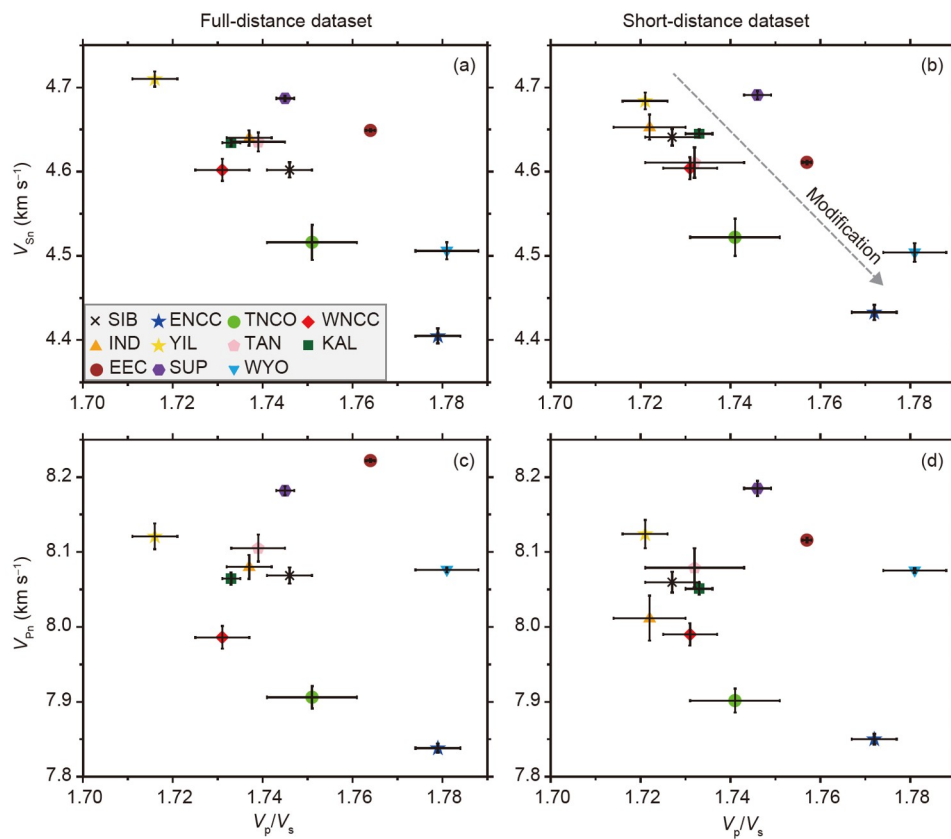


Figure 4 Comparison of the correlation of the seismic properties (V_p/V_s versus V_{Sn} and V_p/V_s versus V_{Pn}) of the cratons estimated from the full-distance dataset (left panel) and short-distance dataset (right panel). Full-distance and short-distance datasets refer to the traveltimes observed in the distance range of 2°–12° and 2°–7°, respectively. In (a) and (b), the ENCC and the Wyoming Craton with high V_p/V_s ratio and low V_{Sn} distinguish themselves from other cratons. The grey arrow in (b) shows a clear trend between the modified and typical cratons.

Supplementary materials. Meanwhile, we should take the following cautions while discussing the results: First, the cratonic blocks are different in size, and this imposes a biased analysis as larger areas have more long rays resulting in higher velocities. To reduce this bias, we also computed the results using short-distance datasets. The short-distance results not

only provide clues about the seismic properties of the shallow parts of the mantle lithosphere, but also evaluate the reliability of the results by presenting a less biased comparison among cratons as well as a different ray distribution. The consistency of the results between full- and short-distance datasets among cratons verifies the reliability of the results. Second, varying

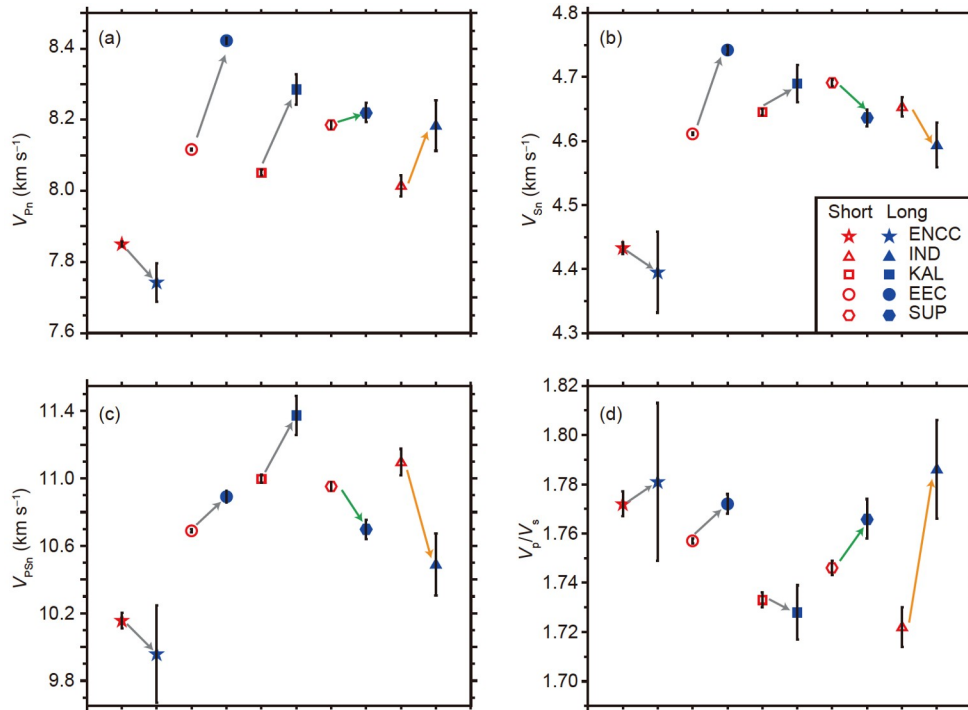


Figure 5 Comparison of the seismic properties (V_{pn} , V_{sn} , V_p/V_s , V_{psn}) of the cratons calculated from the short- and long-distance datasets. Short-distance (red open symbols) and long-distance (blue filled symbols) datasets refer to the traveltimes observed in the distance range of 2° – 7° and 7° – 12° , respectively. The grey arrows display the transitions from short- to long-distance datasets for the Kalahari and East European Cratons, and the green and orange ones show the trends for the Superior and Indian Cratons, respectively. For the Indian Craton, from short- to long-distance datasets, the V_p/V_s ratio increases significantly, and the V_{sn} decreases. These transitions suggest that the deeper parts of the mantle lithosphere beneath the Indian Craton are partially modified. The lowered V_{sn} , as well as a slight change of V_{pn} , of the Superior Craton from short- to long-distance datasets might indicate the partial modification of its deeper parts.

ray coverage leads to somewhat different results due to the heterogeneous nature of the uppermost mantle lithosphere. In order to lessen this effect, we evaluated the consistency of the results by testing various subregions as well as testing them with and without earthquake clusters. Furthermore, we also employed a bootstrap method (Schmidt and Heinson, 2015) to select subsets of data. We applied the same linear regression analysis to these sub datasets and confirmed that our results are robust. Moreover, in this study, we only focused on conspicuous meaningful contrast among results considering their associated uncertainties and skipped discussing less certain observations.

5.2 Comparison with previous studies

Generally, the estimated average Pn and Sn velocities here (Figure 3c–3f) are generally consistent with the published regional Pn and Sn tomography results (e.g., Pei et al., 2007, 2011; Zhang et al., 2009; Buehler and Shearer, 2014, 2017; Sun and Kennett, 2016; Lü et al., 2017, 2020; Lü, 2019; Illa et al., 2021). For example, recent Pn tomography studies for the NCC (e.g., Lü, 2019; Lü et al., 2020) show a complicated and heterogeneous mantle lithosphere beneath NCC, suggesting an average low Pn velocity for the ENCC and TNCO and a higher velocity for the WNCC. Buehler and Shearer

(2014) showed comparatively low V_{sn} ($\sim 4.5 \text{ km s}^{-1}$), high V_{pn} ($\sim 8.1 \text{ km s}^{-1}$), and high V_p/V_s ratio (~ 1.78) for the Wyoming Craton. Pn tomography studies by Buehler and Shearer (2017) and Zhang et al. (2009) suggested a comparatively uniform high Pn velocity ($\sim 8.2 \text{ km s}^{-1}$) for the Superior Craton. Pn and Sn tomography studies (Pei et al., 2011; Lü et al., 2017; Illa et al., 2021) revealed relatively medium to high Pn (~ 8.05 – 8.15 km s^{-1}) and Sn ($\sim 4.6 \text{ km s}^{-1}$) velocities for parts of the Indian cratons. The Pn tomography of Sun and Kennett (2016) showed a relatively uniform high Pn velocity (~ 8.1 – 8.2 km s^{-1}) for the Yilgarn Craton. We noticed some slight inconsistencies between our results and the above studies, which could have stemmed from the following points: First, our results are average apparent velocities, whereas Pn and Sn tomography show velocity perturbation relative to the average velocity, which can be affected by parameterization, regularization, and data weighting scheme. In addition, compared with our study, Pn and Sn tomography due to implementing larger areas tends to include longer rays ($>12^\circ$) and thus generally result in higher velocities. Moreover, the results in this paper are generally in agreement with the surface wave analyses beneath cratons (Lebedev et al., 2009; Pedersen et al., 2009). For example, Pedersen et al. (2009) carried out surface wave analyses in order to compare the Kaapvaal, Finland, Slave,

and Yilgarn Cratons. They presented a higher S-wave velocity of $\sim 4.70 \text{ km s}^{-1}$ for the Yilgarn Craton compared with that of Finland and Kaapvaal Cratons, which are quantitatively and comparatively consistent with our measurements beneath these areas.

5.3 Consistency of the results among most cratons

Except for the ENCC, TNCO, Wyoming, and comparatively the East European Craton, which also includes some Paleoproterozoic crustal parts, other cratonic blocks show comparable velocities and V_p/V_s ratios (Figure 3); For example, this range is $\sim 4.6\text{--}4.7 \text{ km s}^{-1}$ for the S-wave velocity, and $\sim 1.72\text{--}1.75$ for the V_p/V_s ratio. Lee (2003) suggested that V_p/V_s ratio strongly depends on the mantle Mg#, and cratons due to their high Mg# show low V_p/V_s ratio and high velocities. Based on Lee's (2003) study, the impact of 1 Mg# difference on V_p/V_s ratio exceeds that of the several hundred degrees temperature change. In addition, 200°C temperature change can only correspond to around 1% S-wave velocity variation. Moreover, global thermal models (e.g., Artemieva et al., 2006) suggest that the temperature difference of the mantle lithosphere among the assessed cratons barely exceeds 200°C . Orthopyroxene enrichment can decrease the V_p/V_s ratio, but decreases the velocity as well (Baptiste and Tommasi, 2014). In addition, except for the Kalahari and Siberian Cratons, the amount of orthopyroxene enrichment is not anomalously high in cratons worldwide (Carlson et al., 2005). Garnet and clinopyroxene enrichment can also increase the velocities, but increases the V_p/V_s ratio as well (Schutt and Lesher, 2010; Baptiste and Tommasi, 2014). The presence of eclogite can significantly increase the velocity, but also result in an analogous V_p/V_s ratio increase. In addition, the high-density nature of eclogite contradicts the buoyant feature of the mantle lithosphere, and studies suggest that its proportion is limited ($\sim 1\%$) within the mantle lithosphere (Carlson et al., 2005). Therefore, the only conclusive reason for the observed low V_p/V_s ratio and high velocities of most cratons here is the presence of a highly depleted mantle lithosphere with the most resemblance to the original residue from the partial melt extraction of the primitive mantle during the Archean. This observation is also in agreement with mantle xenolith records of the uppermost mantle lithosphere for the cratons, showing a limited Mg# range of ~ 92 to 93 with an average of ~ 92.8 (Bernstein et al., 2007). In addition, this is also consistent with the observation that the cratons due to their higher viscosity maintain good coupling at the Moho boundary (Carlson et al., 2005). Moreover, as illustrated in Figure 4, the contrasting V_p/V_s ratio and S-wave velocity of the ENCC and the Wyoming Craton as the modified cratons indicate that modification is not only confined within the base of the lithosphere. Instead, it can even manifest in the uppermost lithospheric mantle depths.

5.4 The Eastern North China Craton

The ENCC shows the lowest P- and S-wave velocities, as well as a distinguishable high V_p/V_s ratio of ~ 1.78 in both short- and full-distance datasets (Figure 3), suggesting a systematic contrast of its nature compared with the other parts of the NCC, as well as with the other cratons. For example, compared with the Yilgarn Craton, the ENCC shows a $\sim 3\%$ decrease for P-wave velocity, $\sim 5\%$ decrease for S-wave velocity, and a $\sim 3\%$ increase for V_p/V_s ratio using the short-distance datasets. This significant contrast cannot be explained by thermal differences alone, as thermal models of the mantle lithosphere (e.g., Artemieva et al., 2006) show around 200°C temperature change between these areas, and this difference (or even greater) cannot justify this significant velocity and V_p/V_s ratio difference between them. Moreover, the contrasting seismic properties of the ENCC from those of the TNCO and the WNCC also cannot be explained by thermal differences alone, as a recently published paper (Yan et al., 2019) suggests a somewhat homogenous temperature within the uppermost mantle for the entire NCC. Therefore, we believe that a substantial amount of these significant differences should be related to the contrasting nature of the uppermost mantle beneath the ENCC, which is also supported by several seismic and geochemical studies (Zhu et al., 2012; Wu et al., 2019).

One proposed scenario for some of the cratons such as South African, East European, and Slave Cratons is the presence of a depleted Archean mantle lithosphere layer overlying a fertile younger one (Carlson et al., 2005). If such a scenario also applies to the ENCC, then the thinning of the ENCC was entirely resulted from pure shear extension (due to the Pacific subduction rollback) rather than delamination from the lower crust. We thus used the short-distance dataset that samples the uppermost mantle to evaluate the validity of such a scenario and to inspect whether or not a depleted thin Archean layer exists just below the Moho of the ENCC. Such a depleted layer is expected to cause high velocities and a low V_p/V_s ratio. The results of P-wave velocity of $\sim 7.85 \text{ km s}^{-1}$, S-wave velocity of $\sim 4.43 \text{ km s}^{-1}$, and V_p/V_s ratio of ~ 1.77 (Figure 3), however, do not match the expected values and refute the proposed scenario for the ENCC. Nevertheless, from full- to short-distance datasets, the ENCC shows a slight increase in velocities ($\sim 1\%$) and a minor decrease in V_p/V_s ratio ($< 1\%$) (Figure 3), which might imply the possibility of such a scenario at small scale localities beneath the ENCC.

5.5 The Western North China Craton

Compared with the ENCC and TNCO, the WNCC exhibits higher velocities (e.g., compared with the ENCC, P-wave velocity: $\sim 2\%$; S-wave velocity: $\sim 4\%$) and lower V_p/V_s ratio

(e.g., compared with the ENCC, ~2%) (Figure 3), which are comparable with those of the typical cratons. Thus, a typical cratonic mantle lithosphere is inferred for the WNCC. There are no mantle xenolith records within the Ordos Block of the WNCC to confirm this idea. Conversely, a recently published xenoliths study at Langshan and Siziwangqi (Dai et al., 2019), which are located at the northernmost edge of the WNCC refutes this idea by showing a fertile upper mantle, similar to that of the ENCC. On the other hand, seismic studies show somewhat high-velocity anomalies centered at the Ordos Block at uppermost mantle depths (Pei et al., 2007; Tao et al., 2018). By assuming an average Mg# of ~89–90 for the ENCC compiled from the Cenozoic samples published in Zheng et al. (2007), as well as considering a somewhat homogenous temperature beneath the NCC (Yan et al., 2019), the significant difference of the seismic properties between the ENCC and the WNCC predicts a depleted (Mg#>92) upper mantle beneath the Ordos Block.

5.6 Wyoming craton

As illustrated in Figure 3, the Wyoming Craton shows a distinctly high V_p/V_s ratio of ~1.78, almost similar to that of the ENCC. On the other hand, its P-wave velocity is ~3% higher than that of the ENCC and is roughly analogous to that of the typical cratons. This perplexing observation seems to be difficult to explain. However, it might show that the mantle lithosphere preserved there but has been highly modified and refertilized by metasomatism, probably induced by the ascending fluids originating from the underlying Farallon Slab. Due to the small size of the Wyoming Craton, our employed rays were mainly short-distance (2° – 7°) rays, which image depths of ~40–50 km, just beneath the Moho. Recent Pn and Sn tomography analyses using a larger ray distance range (Buehler and Shearer, 2014, 2017) also show high Pn velocity, low Sn velocity, and a high V_p/V_s ratio for the Wyoming Craton, a unique feature within the western United States. Based on the epicentral distance range of their Pn/Sn data, we infer that the distinct velocity structure extends to depths of ~80–90 km. Moreover, comparatively high-velocity anomalies from depths deeper than sensitivity depths of the Pn/Sn to around 200 km revealed by body and surface wave tomography (e.g., Humphreys et al., 2015; Golos et al., 2020) suggest the presence of a comparatively thick lithosphere, which further support our idea about the status of the Wyoming Craton.

5.7 Short-distance and long-distance datasets

Employing short- and long-distance rays permits us to explore the variation of the seismic properties with depth at uppermost lithospheric mantle depths. Here, we have an acceptable number of long-distance rays for the Superior,

East European, and Kalahari Cratons, with fewer ones for the ENCC and Indian Craton. We attribute the short- and long-distance datasets to shallow and deeper parts of the mantle lithosphere. As illustrated in Figure 5, the results using short- and long-distance datasets suggest that cratons seismically behave differently with depth, possibly relating to their particular evolution history. Compared with the Superior and Indian Cratons, the Kaapvaal and East European Cratons show a more similar trend in seismic properties change from the short- to the long-distance datasets (Figure 5). For the Kalahari and East European Cratons, a positive gradient is present for the P- and S-wave velocities (Figure 5). In contrast, the Superior Craton exhibits a negative gradient for the S-wave velocity (~1%) as well as a slight change for the P-wave velocity (Figure 5). A recent study (Smit et al., 2014) suggests that some parts of the mantle lithosphere beneath the Superior Craton were modified during the Mid Continent Rifting. Combining this evidence with our findings contradicts the general belief that the Superior Craton is an intact craton and alternatively proposes a partial modification of its mantle lithosphere at the deeper parts. The Indian Craton in this study comprises parts of the Dharwar, Bastar, and Singhbhum Cratons, as well as the Deccan Traps. Using the short-distance dataset, the velocities and V_p/V_s ratio (~1.72) are somewhat comparable with those of the typical cratons, whereas the seismic properties especially the V_p/V_s ratio using the long-distance dataset differ from those of the typical cratons. As illustrated in Figure 5c, the V_p/V_s ratio from short- to long-distance datasets increases by more than 4% and attains ~1.79, roughly similar to the V_p/V_s ratio of the ENCC. Since the V_p/V_s ratio is a better index for constraining the compositional changes (Lee, 2003), we interpret these features as a scenario of a depleted Archean uppermost mantle lithosphere at shallow parts overlying a fertile younger one at deeper parts beneath the Indian Craton. This scenario is in agreement with the recent mantle xenolith suits from the westernmost side of the Indian craton, which suggests a very thin Archean uppermost mantle overlying a newly accreted fertile one beneath the western parts of the Indian Craton (Dessai et al., 2021), although our larger study area might generalize this scenario for the larger parts of the Indian Craton.

6. Conclusions

We selected 11 cratonic blocks and compared the seismic properties of their uppermost mantle lithosphere to elicit to what degree each craton has been modified since the Archean. We analyzed the Pn, Sn, PSn, and V_p/V_s ratio recorded at short (2° – 7°), long (7° – 12°) (only for larger blocks), and full (2° – 12°) distance ranges and reached the following conclusions:

(1) Most cratons show comparable seismic properties with high velocities and low V_p/V_s ratio, except for the ENCC, TNCO, Wyoming, and to some extent in the East European Craton, which also includes some Paleoproterozoic crustal parts. This observation suggests a highly depleted nature of the mantle lithosphere beneath most cratons that resembles the original residue of the melt-extraction process of the primitive mantle during the Archean.

(2) The ENCC shows the lowest velocities and high V_p/V_s ratios in both the short-distance and full-distance datasets, indicating a systematic difference in its lithospheric mantle nature. This contrast suggests a total removal of the Archean mantle lithosphere beneath the ENCC. In contrast to the ENCC, the low V_p/V_s ratio and high velocities of the WNCC support the presence of the Archean mantle lithosphere beneath it.

(3) The Wyoming Craton displays a high V_p/V_s ratio, comparable to that of the ENCC. It also shows a high P-wave velocity, similar to that of the typical cratons. These features suggest that the Archean mantle lithosphere beneath the Wyoming Craton is still there, but it has been highly modified by metasomatism due to the ascending fluids from the underlying Farallon slab.

(4) Indian Craton in this study includes parts of the Dharwar, Bastar, Singhbhum Cratons, as well as the Deccan Traps. Its low V_p/V_s ratio and high velocities at shallow depths change to a high V_p/V_s ratio (comparable to that of the ENCC) and a lowered V_{Sn} at deeper parts, thus suggesting a partial modification of the deeper parts of the uppermost mantle lithosphere beneath it.

Acknowledgements We thank the China Earthquake Administration (CEA) and International Seismological Centre for providing the Pn and Sn traveltimes data. We also appreciate three anonymous reviewers as well as the responsible editor for their constructive suggestions, which have significantly improved the manuscript. This work was supported by the National Natural Science Foundation of China (Grant Nos. 41630209, U2039203, 42130306).

References

- Artemieva I M. 2006. Global $1^\circ \times 1^\circ$ thermal model TC1 for the continental lithosphere: Implications for lithosphere secular evolution. *Tectonophysics*, 416: 245–277
- Artemieva I M. 2009. The continental lithosphere: Reconciling thermal, seismic, and petrologic data. *Lithos*, 109: 23–46
- Artemieva I M, Thybo H, Cherepanova Y. 2019. Isopycnicity of cratonic mantle restricted to kimberlite provinces. *Earth Planet Sci Lett*, 505: 13–19
- Artemieva I M, Thybo H, Kaban M K. 2006. Deep Europe today: Geophysical synthesis of the upper mantle structure and lithospheric processes over 3.5 Ga. *Memoirs*, 32: 11–41
- Baptiste V, Tommasi A. 2014. Petrophysical constraints on the seismic properties of the Kaapvaal craton mantle root. *Solid Earth*, 5: 45–63
- Bernstein S, Kelemen P B, Hanghøj K. 2007. Consistent olivine Mg# in cratonic mantle reflects Archean mantle melting to the exhaustion of orthopyroxene. *Geology*, 35: 459
- Bruneton M, Pedersen H A, Vacher P, Kukkonen I T, Arndt N T, Funke S, Friederich W, Farra V. 2004. Layered lithospheric mantle in the central Baltic Shield from surface waves and xenolith analysis. *Earth Planet Sci Lett*, 226: 41–52
- Buehler J S, Shearer P M. 2017. Uppermost mantle seismic velocity structure beneath USArray. *J Geophys Res-Solid Earth*, 122: 436–448
- Buehler J S, Shearer P M. 2014. Anisotropy and V_p/V_s in the uppermost mantle beneath the western United States from joint analysis of Pn and Sn phases. *J Geophys Res-Solid Earth*, 119: 1200–1219
- Carlson R W, Irving A J, Schulze D J, Hearn Jr B C. 2004. Timing of Precambrian melt depletion and Phanerozoic refertilization events in the lithospheric mantle of the Wyoming Craton and adjacent Central Plains Orogen. *Lithos*, 77: 453–472
- Carlson R W, Pearson D G, James D E. 2005. Physical, chemical, and chronological characteristics of continental mantle. *Rev Geophys*, 43: RG1001
- Celli N L, Lebedev S, Schaeffer A J, Gaina C. 2020. African cratonic lithosphere carved by mantle plumes. *Nat Commun*, 11: 92
- Chen L, Tao W, Zhao L, Zheng T. 2008. Distinct lateral variation of lithospheric thickness in the Northeastern North China Craton. *Earth Planet Sci Lett*, 267: 56–68
- Chen L, Cheng C, Wei Z. 2009. Seismic evidence for significant lateral variations in lithospheric thickness beneath the central and western North China Craton. *Earth Planet Sci Lett*, 286: 171–183
- Dai H K, Zheng J P, Xiong Q, Su Y P, Pan S K, Ping X Q, Zhou X. 2019. Fertile lithospheric mantle underlying ancient continental crust beneath the northwestern North China craton: Significant effect from the southward subduction of the Paleo-Asian Ocean. *GSA Bull*, 131: 3–20
- Dessai A G, Viegas A, Griffin W L. 2021. Thermal architecture of cratonic India and implications for decratonization of the Western Dharwar Craton: Evidence from mantle xenoliths in the Deccan Traps. *Lithos*, 382–383: 105927
- Eeken T, Goes S, Pedersen H A, Arndt N T, Bouilhol P. 2018. Seismic evidence for depth-dependent metasomatism in cratons. *Earth Planet Sci Lett*, 491: 148–159
- Golos E M, Fang H, van der Hilst R D. 2020. Variations in seismic wave speed and V_p/V_s ratio in the North American lithosphere. *JGR Solid Earth*, 125: e2020JB020574
- Hearn T, Beghoul N, Barazangi M. 1991. Tomography of the western United States from regional arrival times. *J Geophys Res*, 96: 16369–16381
- Hearn T M, Ni J F, Wang H, Sandvol E A, Chen Y J. 2019. Depth-dependent Pn velocities and configuration of Indian and Asian lithosphere beneath the Tibetan Plateau. *Geophys J Int*, 217: 179–189
- Hu J, Liu L, Faccenda M, Zhou Q, Fischer K M, Marshak S, Lundstrom C. 2018. Modification of the Western Gondwana craton by plume-lithosphere interaction. *Nat Geosci*, 11: 203–210
- Humphreys E D, Schmandt B, Bezada M J, Perry-Houts J. 2015. Recent craton growth by slab stacking beneath Wyoming. *Earth Planet Sci Lett*, 429: 170–180
- Illa B, Reshma K S, Kumar P, Srinagesh D, Haldar C, Kumar S, Mandal P. 2021. Pn tomography and anisotropic study of the Indian shield and the adjacent regions. *Tectonophysics*, 813: 228932
- James D E, Boyd F R, Schutt D, Bell D R, Carlson R W. 2004. Xenolith constraints on seismic velocities in the upper mantle beneath southern Africa. *Geochem Geophys Geosyst*, 5: Q01002
- Jiang M, Ai Y, Chen L, Yang Y. 2013. Local modification of the lithosphere beneath the central and western North China Craton: 3-D constraints from Rayleigh wave tomography. *Gondwana Res*, 24: 849–864
- Laske G, Masters G, Ma Z, Pasyanos M E, Livermore L. 2013. Update on CRUST1.0: A 1-degree global model of Earth's crust. *Geophys Res Abstr*, 15: Abstract EGU2013–2658
- Lebedev S, Boonen J, Trampert J. 2009. Seismic structure of Precambrian lithosphere: New constraints from broad-band surface-wave dispersion. *Lithos*, 109: 96–111
- Lee C T A. 2003. Compositional variation of density and seismic velocities in natural peridotites at STP conditions: Implications for seismic ima-

- ging of compositional heterogeneities in the upper mantle. *J Geophys Res*, 108: 2441
- Lei J. 2012. Upper-mantle tomography and dynamics beneath the North China Craton. *J Geophys Res*, 117: B06313
- Lei J, Zhao D, Xu X, Du M, Mi Q, Lu M. 2020. P-wave upper-mantle tomography of the Tanlu fault zone in eastern China. *Phys Earth Planet Inter*, 299: 106402
- Lü Y, Ni S, Chen L, Chen Q F. 2017. Pn tomography with Moho depth correction from eastern Europe to western China. *J Geophys Res-Solid Earth*, 122: 1284–1301
- Lü Y, Xu Y, Liu J, He Y, Zhang J. 2020. Complex deformation of Central and North China through Pn velocity and anisotropy tomography. *Geochem Geophys Geosyst*, 21: e2019GC008661
- Lü Z. 2019. Uppermost mantle velocity and anisotropy structure beneath the North China Craton and its adjacent regions. *Tectonophysics*, 754: 45–55
- Maurya S, Montagner J P, Kumar M R, Stutzmann E, Kiselev S, Burgos G, Rao N P, Srinagesh D. 2016. Imaging the lithospheric structure beneath the Indian continent. *J Geophys Res-Solid Earth*, 121: 7450–7468
- Montgomery D C, Runger G C. 2011. Applied Statistics and Probability for Engineers, 5th ed. New York: Wiley
- Niu F, Levander A, Cooper C M, Lee C T A, Lenardic A, James D E. 2004. Seismic constraints on the depth and composition of the mantle keel beneath the Kaapvaal craton. *Earth Planet Sci Lett*, 224: 337–346
- Niu Y, Liu Y, Xue Q, Shao F, Chen S, Duan M, Guo P, Gong H, Hu Y, Hu Z, Kong J, Li J, Liu J, Sun P, Sun W, Ye L, Xiao Y, Zhang Y. 2015. Exotic origin of the Chinese continental shelf: New insights into the tectonic evolution of the western Pacific and eastern China since the Mesozoic. *Sci Bull*, 60: 1598–1616
- Pearson D G, Scott J M, Liu J, Schaeffer A, Wang L H, van Hunen J, Szilas K, Chacko T, Kelemen P B. 2021. Deep continental roots and cratons. *Nature*, 596: 199–210
- Pedersen H A, Fishwick S, Snyder D B. 2009. A comparison of cratonic roots through consistent analysis of seismic surface waves. *Lithos*, 109: 81–95
- Pei S, Zhao J, Sun Y, Xu Z, Wang S, Liu H, Rowe C A, Toksöz M N, Gao X. 2007. Upper mantle seismic velocities and anisotropy in China determined through Pn and Sn tomography. *J Geophys Res*, 112: B05312
- Pei S, Sun Y, Toksöz M N. 2011. Tomographic Pn and Sn velocity beneath the continental collision zone from Alps to Himalaya. *J Geophys Res*, 116: B10311
- Schnaidt S, Heinson G. 2015. Bootstrap resampling as a tool for uncertainty analysis in 2-D magnetotelluric inversion modelling. *Geophys J Int*, 203: 92–106
- Schutt D L, Leshner C E. 2010. Compositional trends among Kaapvaal Craton garnet peridotite xenoliths and their effects on seismic velocity and density. *Earth Planet Sci Lett*, 300: 367–373
- Shapiro N M, Ritzwoller M H. 2002. Monte-Carlo inversion for a global shear-velocity model of the crust and upper mantle. *Geophys J Int*, 151: 88–105
- Shulgin A, Artemieva I M. 2019. Thermochemical heterogeneity and density of continental and oceanic upper mantle in the European-North Atlantic Region. *J Geophys Res-Solid Earth*, 124: 9280–9312
- Smit K V, Pearson D G, Stachel T, Sellar M. 2014. Peridotites from Atwapiskat, Canada: Mesoproterozoic reworking of palaeoarchaean lithospheric mantle beneath the northern superior superterrane. *J Petrol*, 55: 1829–1863
- Sun W, Kennett B L N. 2016. Uppermost mantle structure of the Australian continent from Pn traveltime tomography. *J Geophys Res-Solid Earth*, 121: 2004–2019
- Tao K, Grand S P, Niu F. 2018. Seismic structure of the upper mantle beneath Eastern Asia from full waveform seismic tomography. *Geochem Geophys Geosyst*, 19: 2732–2763
- Wang X, Zhu P, Kusky T M, Zhao N, Li X, Wang Z. 2016. Dynamic cause of marginal lithospheric thinning and implications for craton destruction: A comparison of the North China, Superior, and Yilgarn Cratons. *Can J Earth Sci*, 53: 1121–1141
- Wu F Y, Yang J H, Xu Y G, Wilde S A, Walker R J. 2019. Destruction of the North China Craton in the Mesozoic. *Annu Rev Earth Planet Sci*, 47: 173–195
- Wu F Y, Xu Y G, Zhu R X, Zhang G W. 2014. Thinning and destruction of the cratonic lithosphere: A global perspective. *Sci China Earth Sci*, 57: 2878–2890
- Xu Q, Liu J, He H, Zhang Y. 2019. Nature and evolution of the lithospheric mantle revealed by water contents and He-Ar isotopes of peridotite xenoliths from Changbaishan and Longgang basalts in Northeast China. *Sci Bull*, 64: 1325–1335
- Xu X, Zhao L, Wang K, Yang J. 2018. Indication from finite-frequency tomography beneath the North China Craton: The heterogeneity of craton destruction. *Sci China Earth Sci*, 61: 1238–1260
- Yan D, Tian Y, Zhao D, Liu C, Zhu H, Li H. 2019. Upper mantle temperature structure of the North China Craton. *Phys Earth Planet Inter*, 293: 106269
- Yu Y, Chen Y J. 2016. Seismic anisotropy beneath the southern Ordos block and the Qinling-Dabie orogen, China: Eastward Tibetan asthenospheric flow around the southern Ordos. *Earth Planet Sci Lett*, 455: 1–6
- Zhang Q, Sandvol E, Liu M. 2009. Tomographic Pn velocity and anisotropy structure in the central and eastern United States. *Bull Seismol Soc Am*, 99: 422–427
- Zhao L, Allen R M, Zheng T, Hung S H. 2009. Reactivation of an Archean craton: Constraints from P- and S-wave tomography in North China. *Geophys Res Lett*, 36: L17306
- Zhao L, Allen R M, Zheng T, Zhu R. 2012. High-resolution body wave tomography models of the upper mantle beneath eastern China and the adjacent areas. *Geochem Geophys Geosyst*, 13: Q06007
- Zheng J P, Griffin W L, O'Reilly S Y, Yu C M, Zhang H F, Pearson N, Zhang M. 2007. Mechanism and timing of lithospheric modification and replacement beneath the eastern North China Craton: Peridotitic xenoliths from the 100 Ma Fuxin basalts and a regional synthesis. *Geochim Cosmochim Acta*, 71: 5203–5225
- Zheng T, Zhu R, Zhao L, Ai Y. 2012. Intralithospheric mantle structures recorded continental subduction. *J Geophys Res*, 117: B03308
- Zhu R, Zhang H, Zhu G, Meng Q, Fan H, Yang J, Wu F, Zhang Z, Zheng T. 2017. Craton destruction and related resources. *Int J Earth Sci-Geol Rund*, 106: 2233–2257
- Zhu R X, Xu Y G, Zhu G, Zhang H F, Xia Q K, Zheng T Y. 2012. Destruction of the North China Craton. *Sci China Earth Sci*, 55: 1565–1587
- Zuo J, Wang L, Niu F. 2020. Multiple source downwellings beneath eastern North China revealed by 3-D CCP migration of receiver function data. *J Asian Earth Sci*, 192: 104266

(Responsible editor: Ling CHEN)